JOURNAL OF THERMOPHYSICS AND HEAT TRANSFER
Vol. 24, No. 2, April–June 2010

Nonequilibrium Radiation Intensity Measurements in Simulated Titan Atmospheres

Aaron M. Brandis,* Richard G. Morgan,† Timothy J. McIntyre,‡ and Peter A. Jacobs§
University of Queensland, Brisbane, Queensland 4072, Australia

DOI: 10.2514/1.44482

This paper details the experimental work conducted at the University of Queensland to measure the nonequilibrium radiation intensity behind a shock in simulated Titan atmospheres, as would be seen during planetary entry. Radiation during Titan entry is more important at lower speeds (about 5–6 km/s) than other planetary entries due to the formation of cyanogen in above equilibrium concentrations in the shock layer, which is a highly radiative species. The experiments were focused on measuring the nonequilibrium radiation emitted from cyanogen between the wavelength range of 310–450 nm. This paper includes experimental results for radiation and spectra found in the postshock region of the flow. Experiments have been conducted at various ambient pressures, shock speeds, and chemical compositions. This leads to a comprehensive benchmark data set for Titan entry, which will be useful for validation of theoretical models. Spectra were recorded at various axial locations behind the shock, enabling the construction of radiation profiles for Titan entry. Furthermore, wavelength profiles can also be constructed to identify various radiating species, in this case, predominately cyanogen violet. Furthermore, this paper includes comparisons with experiments performed at NASA Ames Research Center on their electric arc-driven shock tube in Titan compositions. Excellent quantitative agreement has been obtained between the two facilities.

I. Introduction

THE design of aeroshells for Titan aerocapture requires reliable estimates of the total heat transfer to the vehicle surface. Present estimates of the heat transfer from computational fluid dynamics (CFD) analyses vary greatly [1], and design uncertainty factors related to thermal protection systems can be very large (more than 100%), as discussed in Gnoffo et al. [2]. In the case of entry into the Titan atmosphere composed predominantly of nitrogen with small amounts of methane, the cyanogen (CN) molecule forms and reaches superequilibrium concentrations in the shock layer and this is known to be a strong radiator [1]. However, the modeling associated with this strong radiator suffers from at least two difficulties: 1) the kinetics of CN excited state populations are not well quantified [1,3,4], and 2) given accurate CN excited states, there is disagreement in the literature about appropriate radiation transport models [4–6]. The models used for the various processes and the coupling between models have a strong influence on the predicted radiative heating levels. To reduce the uncertainty and variation among the CFD analyses, it is therefore important to perform experiments that study the shock-layer flow over aeroshell vehicles in a simulated Titan atmosphere. This paper presents measurements of radiation emitted from an impulsive test flow generated using a superorbital nonreflected shock tube. The flow in the facility simulates Titan entry conditions at different speeds and altitudes, including chemical nonequilibrium effects. Optical diagnostics are used to monitor the history of the radiation as well as its spectral distribution over the range 310–450 nm. Calibration allows absolute power densities to be obtained, which are compared to similar measurements from the NASA Electric Arc Shock Tube (EAST) facility [3]. The measurements are also suitable for comparison with future numerical simulations of the flow.

Presented as Paper 4136 at the 26th AIAA Aerodynamic Measurement Technology and Ground Testing Conference, Seattle, WA, 23–26 June 2008; received 20 March 2009; revision received 16 September 2009; accepted for publication 30 September 2009.

*Ph.D. Research Student. Member AIAA.
†Director Centre of Hypersonics. Member AIAA.
‡Senior Lecturer, School of Mathematics and Physics. Member AIAA.
§Senior Lecturer, Mechanical Engineering Department.

II. Previous Radiation Testing in Shock Tubes

Experimental investigations of nonequilibrium radiation in shock tubes have previously been performed by a number of institutions, including NASA Ames Research Center in California [3,7] and Université de Provence in Marseilles, France [8]. NASA Ames uses an electric arc-driven shock-tube facility known as EAST [7], whereas Université de Provence's tests were performed on a free-piston-driven shock tube based on the Stalker [9] principle (the same principle behind the X2 shock tube), known as TCM2 [8].

NASA Ames Research Center has conducted several experiments to measure the radiation behind a shock under different atmospheric conditions [7]. Tests for entry into the atmospheres of the Earth, Mars, Titan, and Neptune were performed in the EAST facility. Shock velocities ranged from 6 km/s for Titan entry conditions up to 34 km/s for Neptune entry conditions. Table 1 shows the test gases, driven tube pressures, and nominal shock velocities covering the majority of the radiation testing performed on EAST.

Experiments have also been performed on Université de Provence's TCM2 facility to evaluate the radiative heat flux during the entry of the Huygens space probe into the atmosphere of Titan. Time resolved emission of CN and C_2 molecules were studied behind a strong shock with the CN violet, C_2 Swan, and CN red radiative systems being examined. The conditions that were used during this testing are presented in Table 2. The Yelle nominal, maximal, and minimal refer to the defined limits of Titan's atmospheric properties as presented in the engineering models developed by Yelle [10].

III. Facility/Test Conditions

A. Facility Conditions

The experiments presented in this paper were carried out in the X2 high-enthalpy shock-tube facility at The University of Queensland. A schematic of X2 is given in Fig. 1, with the most important dimension with regards to the experimental testing being the bore of the acceleration tube, which is 85 mm. Previously, X2 has generally been operated as an expansion tube; however, for these experiments, the facility was modified to be operated as a nonreflected shock tunnel (NRST). In this configuration, the free-piston driver is used to generate a strong shock wave that passes through the stagnant test gas

Table 1 NASA Ames EAST testing conditions [7]

Planet	Test gas (mole fraction)	Pressure, Pa	Nominal shock speed, km/s
Earth	Air	13.3, 26.6, 39.9, 93.1, and 133	10.0
Mars	$0.96\,CO_2/0.04\,N_2$	13.3	8.5
Titan	$0.98\,N_2/0.02\,CH_4$	13.3, 133	5.7

Table 2 Université de Provence TCM2 testing conditions [8]

Planet	Test gas (mole fraction)	Pressure, Pa	Nominal shock speed, km/s
Titan (TCM2 classical)	$92\%\,N_2/3\%\,CH_4/5\%$ Ar	50, 200, 1100	5.5
Titan (Yelle nominal)	$95\%\,N_2/3\%\,CH_4/2\%$ Ar	50, 200	5.5
Titan (Yelle mininum)	$95\%\,N_2/5\%\,CH_4/0\%$ Ar	50, 200	5.5
Titan (Yelle maximum)	$89\%\,N_2/1\%\,CH_4/10\%$ Ar	50, 200	5.5

in the shock tube. The shock leaves the tube as a planar wave and the heated test gas behind the shock front simulates conditions behind the bow shock on a reentry vehicle. This enables the experiments to be performed with flow parameters, such as velocity, static pressure, and atmospheric composition close to actual Titan flight conditions. As the tests are performed at real flight pressures, full-capsule geometry must be used if it is intended to test aerodynamic features of the flow. Because of the small region of test gas in a nonreflected shock tube, they are therefore not suitable for reproducing the aerodynamic flowfield, just a small region of the flow where it is radiating. To date, there have been relatively few attempts to measure the radiative intensity for Titan entry conditions. The shock tunnels at The University of Queensland use free-piston driver techniques to provide a very consistent and uniform test flow. Because of this driver arrangement, combined with the ability to produce high-enthalpy conditions, The University of Queensland shock tubes are among the few facilities around the world capable of replicating these high-velocity radiating flows.

B. Test Conditions

The conditions used for this testing campaign were designed to provide a comprehensive benchmark data set for Titan entry. The experiments were undertaken to determine the effects of velocity, pressure, and gas composition on radiation intensity. Therefore, several shots were performed with one parameter systematically changed between experiments and all others kept constant. For the experiments presented in this paper, the facility was configured as follows:

1) The driver was a mixture of helium and argon initially contained within the compression tube, the relative amounts of each depending on the desired test condition, at a pressure of 30 kPa before compression.

2) The Titan gas used in these experiments was generally made up of 98% N_2 and 2% CH_4, giving the closest match to the lunar atmosphere. Additionally, tests were performed with other CH_4 concentrations to investigate its effect on the radiation intensity. This test gas initially fills the shock tube and test section.

3) The primary diaphragm separating the two gas mixtures was prescored 1.2 mm steel, which ruptures at approximately 15.5 MPa.

Across the large number of shots (and in many cases, several repeated shots), the shock velocities were approximately within $\pm 2\%$ of the nominal values indicated in Fig. 2 and measured to an accuracy of 1% for each experiment. The typical test time for each shot was about 50 μs; the actual value is dependent on the condition and was measured experimentally during each test. For the full set of test conditions used in the shock-tube experiments performed during this campaign, refer to Fig. 2.

C. Optical Arrangement

The optical arrangement during these experiments was designed to allow the recording of the radiation emitted from the hot test gas immediately following the shock front. Spectral information was recorded using a Princeton Instruments ACTON Spectra Pro 2300i 300 mm focal length imaging, triple grating monochromator/spectrograph coupled to a gated intensified charge coupled device (ICCD). A 600 lines/mm grating was used in the spectrometer giving a spectral resolution of 0.137 nm/pixel. An entrance slit width of 100 μm was used throughout the experiments. The focusing optics consisted of a periscope mirror arrangement, a 100 mm focal-length lens, and an aperture set at a radius of 6.5 mm, as shown in Fig. 3. The periscope mirror arrangement was used to rotate the emitted radiation beam from the test section and align it with the spectrometer slit (which is perpendicular to the flow direction). The resulting demagnification was approximately a factor of 12.1, resulting in 84 mm of flow captured during each 100 ns exposure of the ICCD camera. The two-dimensional captured data gives intensity over a range of wavelengths at axial locations down the centerline of the test section. A Shimadzu HPV-1 camera capable of recording 100 frames at a rate of up to 1 MHz was also used to observe the experimental flow. This provides information regarding the uniformity of the flow, the test time (as the interface between the driver and test gases can be seen), and the steadiness of the flow during the test time. The ICCD camera and the high-speed camera were triggered with a signal from a photodiode looking through the window of the test section. This photodiode triggering system enabled us to accurately capture the flow area of interest.

IV. Experimentation

A. Flow Quality

To quantify the quality of the flow, pitot pressure survey shots were performed. Sample pitot traces for two repeat shots, with three transducers on each run spaced 17.5 mm apart and located at an axial station 25 mm from the tube exit are presented in Fig. 4. This demonstrates the repeatability and uniformity of the flow for the first 45 μs containing the test period. The level region between 14 and 60 μs indicates the steady flow. Driver gas arrival and flow termination is shown by the sudden rise in pitot pressure after 60 μs.

The temporal evolution of the flow was also examined using high-speed photography with a Shimadzu HPV-1 camera, with the light source being the flow luminosity. A number of frames from the high-speed camera are shown in Fig. 5. Various frames are shown at this condition with their corresponding time indicated on a pitot trace.

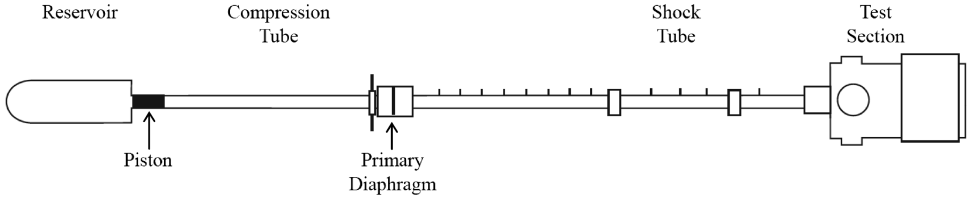

Fig. 1 Schematic of NRST X2 configuration [19].

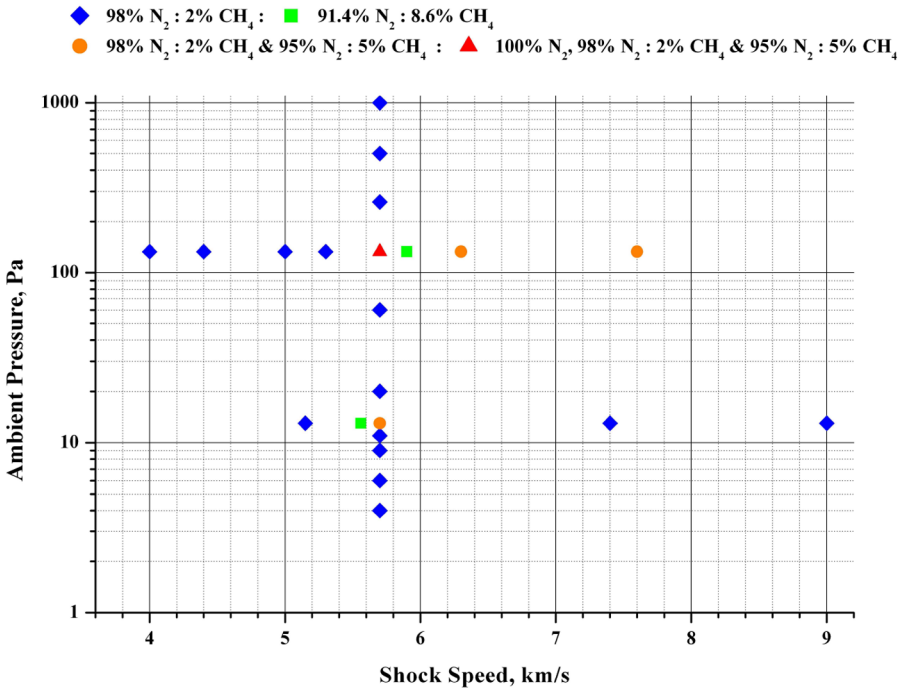

Fig. 2 X2 experimental matrix.

The pitot trace has a steady period of about 45 μs (so we have a length of radiating test gas of about 250 mm). The shock can be seen leaving the tube exit and traversing the region captured by the high-speed camera. Behind the shock, the radiating test gas can be seen. As time progresses the intensity of the radiating test gas decreases, and this is reflected in the reducing light shown. In the last frame, the collapse of the steady radiating flowfield indicates that the interface between the (cooler) driver gas and (hotter) test gas has arrived. This gives further validation to the test time of the experiment the data from the high-speed camera correlates very well with the pitot trace.

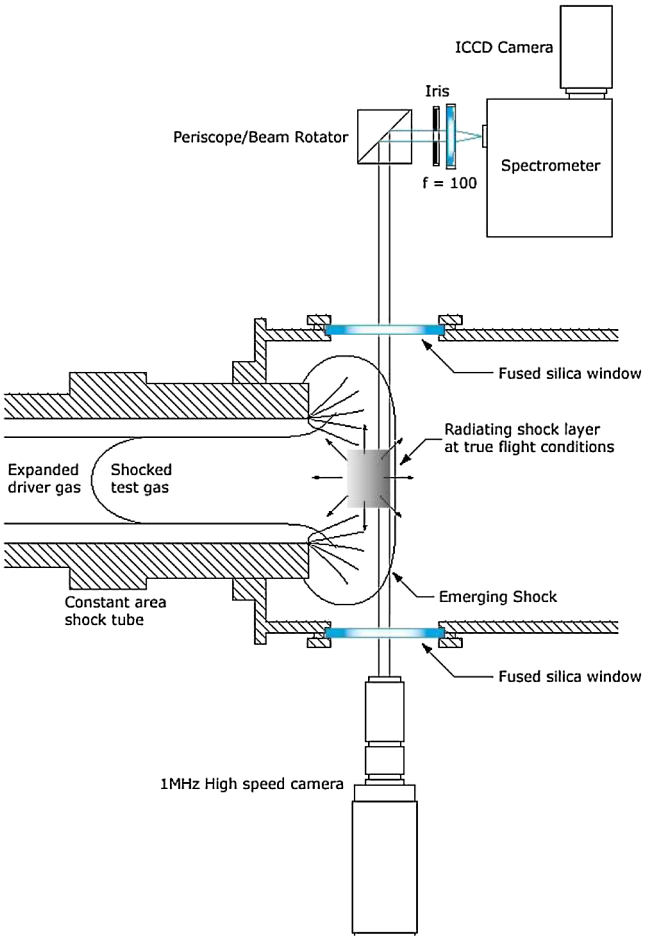

Fig. 3 Plan view of the X2 optical arrangement. Flow from the shock tube travels from left to right in this figure, with the shock shown just after it emerges from the shock tube.

B. Contamination

Contamination is a major concern when it comes to radiation testing. Impurities can interrupt the flow in many ways. Impurities can emit radiation or dissociate and form unwanted molecules via reactions with the test gas and interrupt the chemical-reaction scheme. To achieve several experiments in one day with the current seals and pumping equipment, evacuating the tunnel down to a very low vacuum ($\ll$ 0.1 Pa) was not possible. The vacuum level that was achieved was typically 0.2–0.3 Pa. However, extra precautions were taken in order to minimize the amount of contamination in the test gas. This included filling the tunnel to a relatively high pressure with the test gas (usually in the order of 1 kPa, significantly higher than the

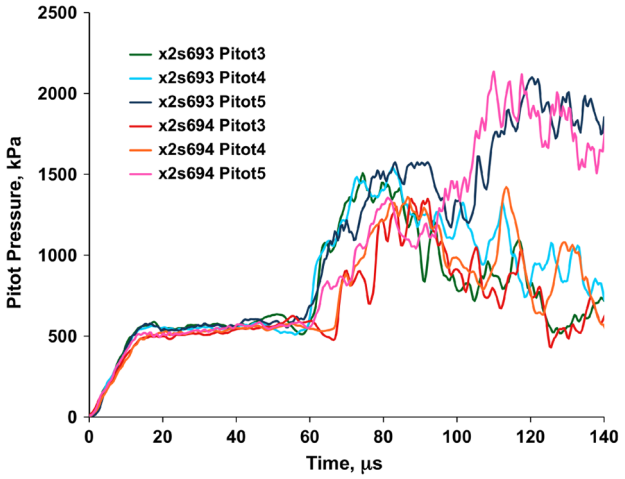

Fig. 4 Sample pitot traces for two repeat shots with three transducers shown for each shot. Pitot5 corresponds to the pitot at the centerline of the flow. Pitot4 and pitot3 are 17.5 and 35 mm above pitot5, respectively. These traces were measured at 5.7 km/s, 133 Pa, and 98% N_2:2% CH_4.

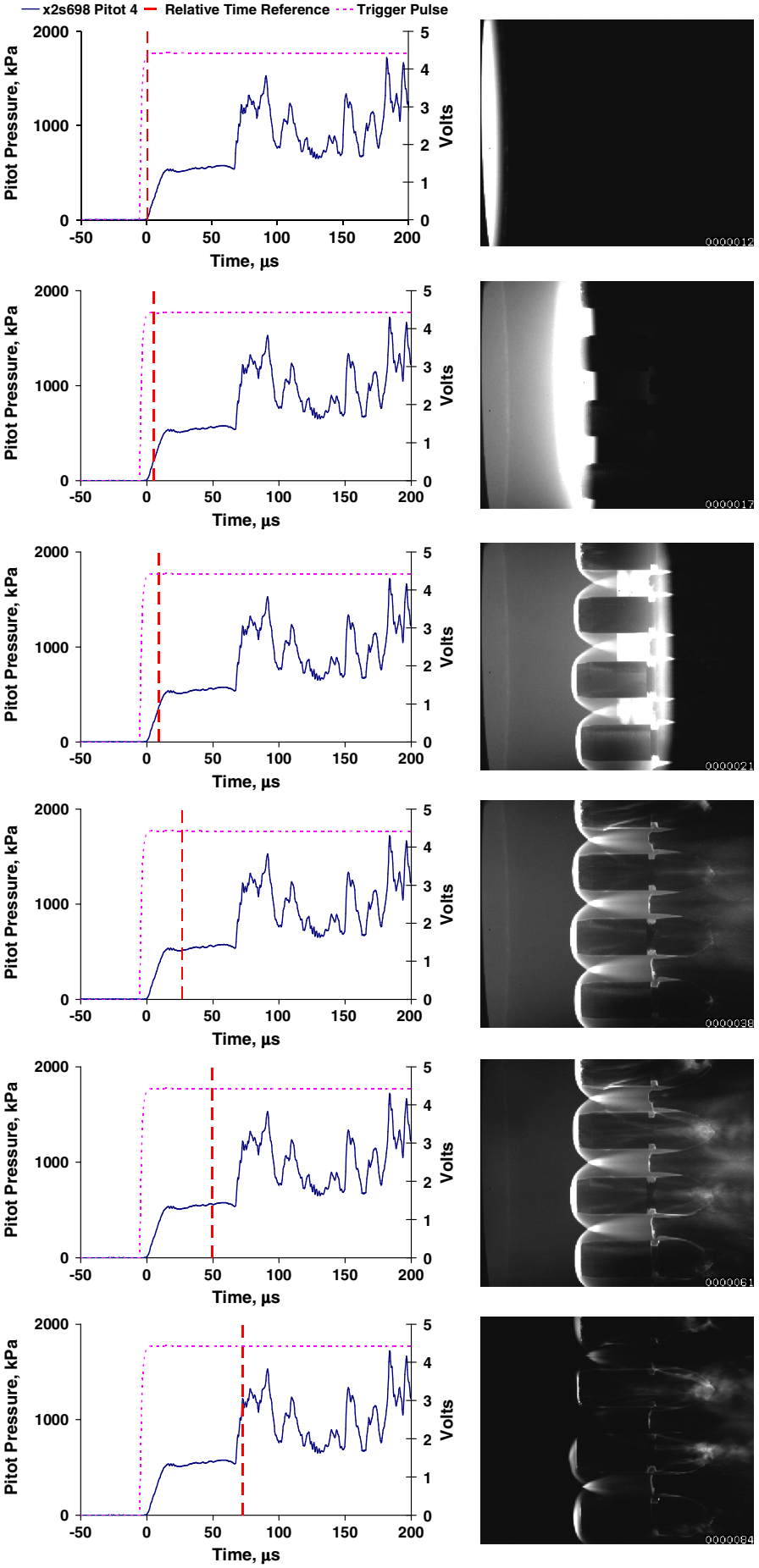

Fig. 5 High-speed-camera data relative to pitot pressure trace for shot x2s698 showing the shock traverse (from left to right) a pitot rake setup in the test flow. The short-dash line is the trigger pulse. The vertical long-dash line indicates the current time of the corresponding image. The solid line is the pitot trace.

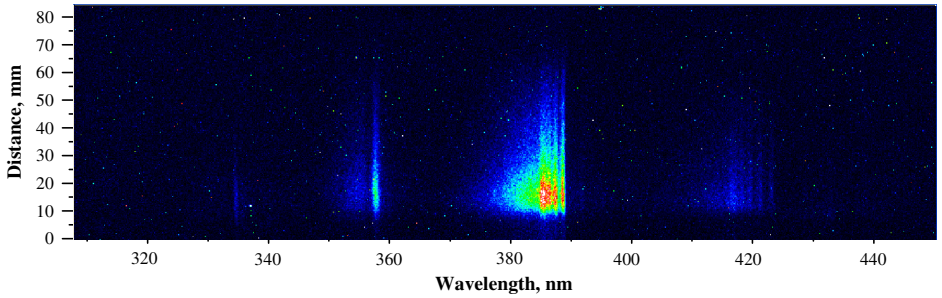

Fig. 6 Raw picture taken for x2s691 in false color.

test gas fill pressure for the shot). The tunnel would then be evacuated again to 0.2–0.3 Pa. At this stage, the majority of the residual gas in the tunnel is now the test gas. However, at this pressure a significant source of the pressure reading could also be attributed to water vapor outgassing from the tube walls. The rate at which the pressure rises when the vacuum pump is isolated from the tunnel just before the shot is fired was measured to be approximately 0.5 Pa/ min. Because of the small time this takes (conservatively 15 s), the amount of contamination during this time is a combination of approximately 0.125 Pa of air and outgassed water vapor. However, as the gauge calibration is gas dependent at these pressures, it is hard to provide definitive levels of air and outgassed water-vapor contamination. So, therefore, it could be said that, conservatively, there may be up to 0.5 Pa of water vapor and/or air contamination in the tube, which corresponds to 500–100,000 ppm of impurity gas depending on the condition.

C. Emission Spectroscopy: Calibration Process

A sample image from the ICCD camera coupled to the spectrometer is shown in Fig. 6. The horizontal axis gives wavelength, the vertical axis is distance behind the shock front (shock at the bottom), and color indicates the intensity per pixel. The three main vibrational transitions of CN are clearly identifiable in the spectrum. The predominant vibrational manifold is $\Delta v = 0$, and the smaller vibrational manifolds either side are $\Delta v = \pm 1$. The transition NH(X–A) can also been seen at about 336 nm, although at a much lower intensity than the CN bands. At present, this is the only wavelength region to be examined in detail.

The intensity measured on the camera in its raw form is given in counts, which is the output from the 16-bit sensor that forms each pixel. A count corresponds to a certain amount of radiative energy that is incident on the pixel. Minimal postprocessing is applied to the raw data from a shock-tube test. Hot pixels (lone pixels that occasionally produce an arbitrary high signal) are removed, and an averaged zero level in front of the shock because of the camera dark count is subtracted from all the data points. To obtain the relationship between counts and energy, a tungsten–halogen OL200M spectral-calibration lamp from Optronic Laboratories was placed 500 mm from the entrance slit of the spectrometer (without intervening optics) and an image recorded. The lamp is provided with calibration data that gives the power per unit area per unit wavelength at the entrance to the spectrometer. This allows a relationship between the amount of energy entering the spectrometer and the counts on the camera to be established. By dividing the counts recorded in a test by the counts from the calibration image and multiplying by the lamp calibration factor, we can then establish the energy recorded in the test provided the relative exposure time and spectrometer entrance slit width between shot and calibration are taken into account. A final correction is then made to account for the magnification of the optics, the losses through the optics and the captured solid angle used in the test. This gives a measurement of spectral radiance ($\mathrm{W/cm^2/\mu m/sr}$) for each pixel on the camera. For better comparison between facilities, the width of the flow is also taken into account by quoting results in the form of a spectral power density ($\mathrm{W/cm^3/\mu m/sr}$) or integrated power density ($\mathrm{W/cm^3/sr}$). This process is represented by the following equations:

$$\Omega = \pi \times \frac{r_a^2}{d_a^2} \qquad L_\lambda = \frac{D_s}{D_c} \times \frac{C_L}{\omega} \times \frac{1}{M_D^2 \times L_o} \times \frac{1}{\Omega}$$

where Ω (sr) is the solid angle, r_a is the radius of the aperture, d_a is the distance to the aperture, L_λ is the spectral radiance, D_s is the zeroed shot data (counts), D_c is the zeroed calibration data (counts), C_L is the lamp output ($\mathrm{W/cm^2nm}$), M_D is the demagnification, L_o is the optical losses, and w (cm) is the flow width.

The optical arrangement is designed so that an image of the centerline of the flow is formed on the entrance slit of the spectrometer. The position of the shock front in the image is set by choosing the delay to trigger the camera as the shock traverses the field of view. For each pixel along the spatial axis of the camera image (which corresponds to about 0.3 mm in the test section), the effective field of view is deep and extends beyond the core flow in both directions. Therefore, the radiation incident on each pixel results from an integrated level of radiation emitted across the whole depth of view, including the uniform test core, and the peripheral regions containing the curved exit shock, as was shown in Fig. 3. To obtain an absolute value for the intensity of the radiation per unit volume, it is assumed that the signal in the image is dominated by the radiation originating in the test core, which has an estimated width of 60 mm along the line of sight of the optics. Experiments and simulations were conducted to test the validity of this assumption.

An error analysis has been performed on the absolute calibration for determining the radiative intensity. Five factors have been identified as the most influential in terms of calculating the level of uncertainty. These factors are the aperture radius, the distance to the iris from the centerline of the tunnel, the width of the core radiating gas, the optical magnification, and the optical losses in the system. Using the combination of uncertainties method demonstrated in Mee [11], the overall uncertainty in the absolute calibration comes out to be ±28%. In the case of repeated shots where the ambient pressure, shock speeds, test-gas composition, and driver conditions are nominally the same; variation in the absolute level of emitted

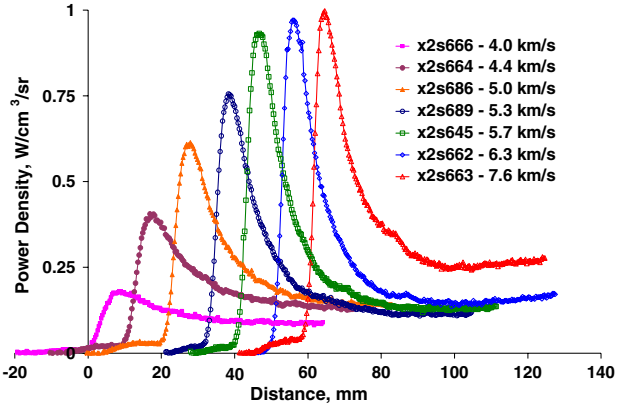

Fig. 7 Peak power density as a function of distance behind the shock for various incident shock velocities integrated across a wavelength region of 310–450 nm. The pressure was held constant at 133 Pa while the gas composition was 98%N_2:2%CH_4. Each graph has been offset horizontally for visual clarity.

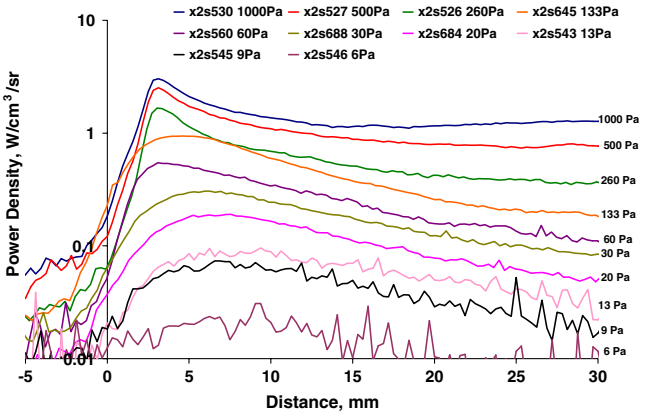

Fig. 8 Peak power density as a function of distance behind the shock for various incident static pressures integrated across a wavelength region of 310–450 nm. The shock speed was held constant at 5.7 km/s while the gas composition was 98%N_2:2%CH_4.

radiation can vary from shot to shot. The reason for this variation has not been established and so a shot-to-shot variation of ±15% has been used to bound the experimental values. When the error in the calibration is combined with the shot-to-shot variation using a sum of squares approach [11,12], the overall uncertainty in the radiation intensity behind the shock is ±31%.

D. Emission Spectroscopy: Experimental Results

Images such as that shown in Fig. 6 were recorded over the range of test conditions given in Fig. 2. Each image was converted to an absolute power density using the calibration process. To compare results across different tests, the images were further reduced to give the maximum power density integrated over a wavelength range of 310–450 nm as a function of distance behind the shock or as a function of wavelength. The power density from the radiating gas was measured as a function of shock velocity, test-gas pressure, and test-gas composition. Figure 7 shows how the power density varies with shock speed. In this data set of experiments, the static pressure was kept constant at 133 Pa and at a composition of 98%N_2:2%CH_4 (within error bounds of 2.2% CH_4 and 1.8% CH_4), with the shock speed varying from 4.0 to 7.6 km/s. The shock speed was controlled by the composition of the driver gas. In the case of the slower shots, there was a large percentage of argon gas used. As the shots became faster, the percentage of helium was increased, up to 100% for the 7.6 km/s condition.

Figure 8 shows how the power-density radiation varies with static pressure. In this set of experiments, the shock speed was kept constant at 5.7 km/s (within 2%) and a composition of 98%N_2:2%CH_4, with the static pressure systematically changed from 6 to 1000 Pa. The driver composition again had to be altered to keep the shock speed constant. The higher the static pressure, the more helium required to drive the shock at 5.7 km/s. Precursor radiation has also been seen during the testing, as is indicated by the small rise in power density before the shock location. This is likely due to ionization of the gas ahead of the shock. It should also be noted that with the spectrometer settings and optical arrangement used during this experimental campaign, the lower limit of power density that could be measured was approximately 0.01 W/cm^3/sr. Wavelength profiles at the peak radiating location for representative conditions of the experimental testing are presented in Fig. 9.

As an example of how this data can be used for validation purposes, the peak power-density values for each of the different shock speeds and static pressures is plotted in Fig. 10. By

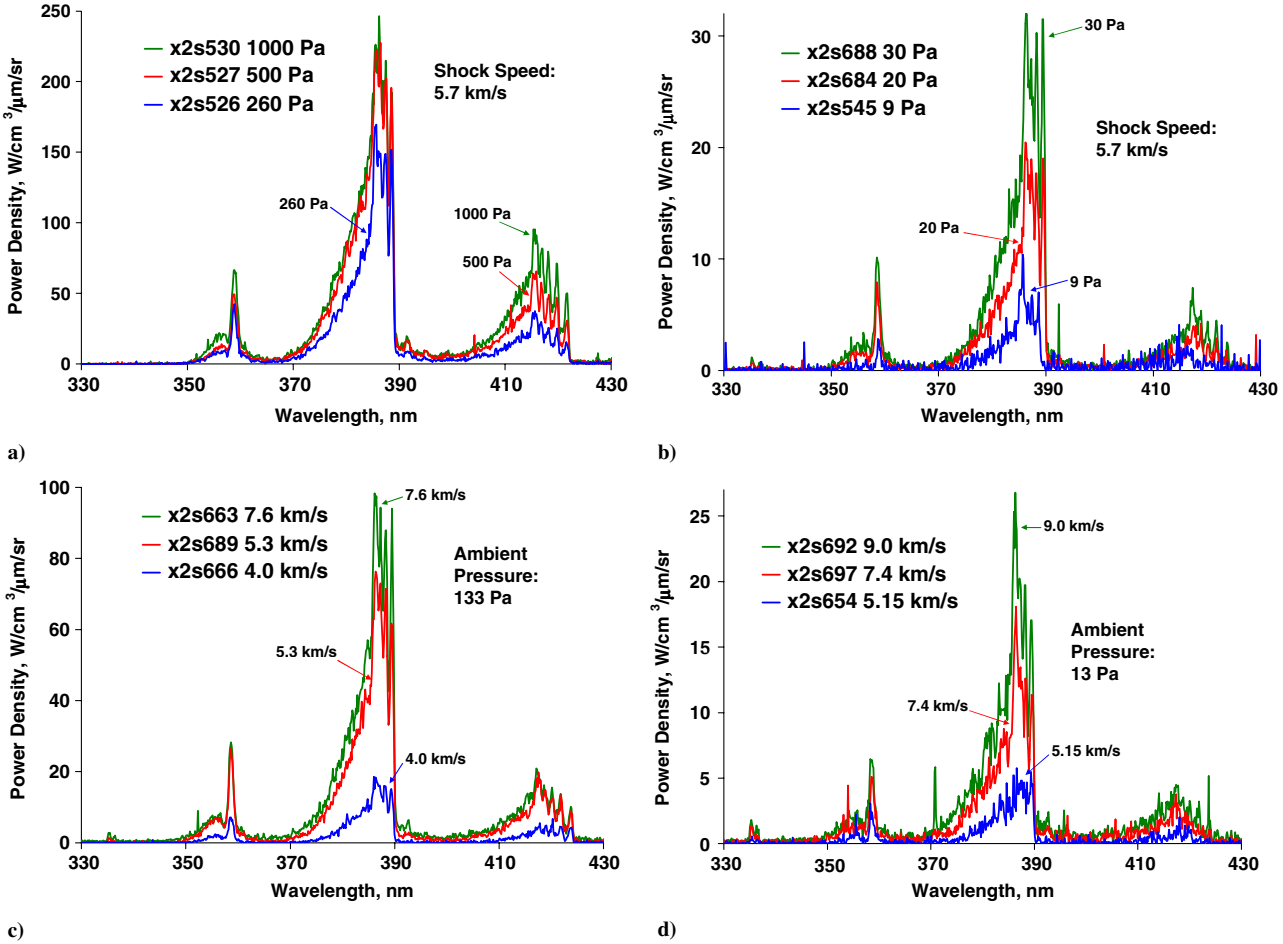

Fig. 9 Spectral profiles at the peak radiation location with a composition of 98%N_2:2%CH_4: a–b) different pressures at a constant velocity. c–d) different shock speeds at a constant pressure.

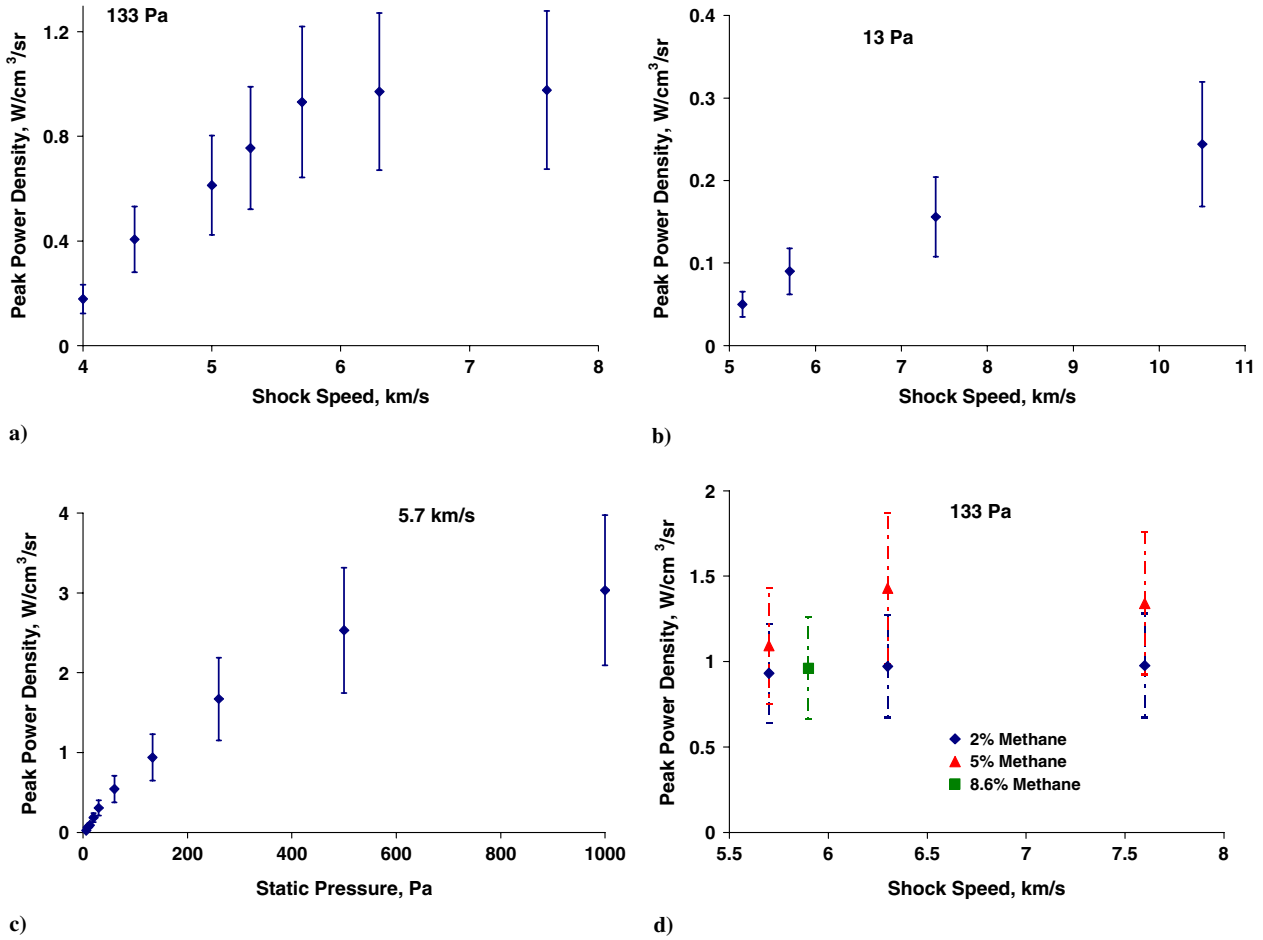

Fig. 10 Peak power density (integrated over 310–450 nm) variation with a–b) shock speed at 98%N_2/2%CH_4, (c) static pressure at 98%N_2/2%CH_4, and (d) CH_4 concentration and shock speed.

representing the data this way, trends in the data can be seen. CFD codes can then be run to simulate the radiation intensity for the various shock-speed and static-pressure initial conditions. If the trend and absolute levels of the CFD agree well with the experimental data, then it provides some confidence that the simulations correctly model the chemistry, shock-tube flow, and corresponding irradiance.

The data suggests that the peak power density is initially linear with shock speed; however, at about 5.7 km/s in the 133 Pa set of experiments, it appears that the peak power density starts to reach a limit and the radiation no longer continues to increase with shock speed (see Fig. 10a). Figure 10b shows the dependence of peak power density against shock speed at 13 Pa. The trend of reaching a limit is not seen; however, this may be due to not enough data points at this condition. The peak power density appears to show a similar trend with static pressure, as was shown with the variation with shock speed. The radiation intensity seems to be initially linear with static pressure, and then with the ambient pressure at about 500 Pa, the radiation seems to reach a limit (see Fig. 10c). The analysis of the reasons behind the nonlinearity with respect to shock speed and ambient pressure are nontrivial, and thus will be discussed in a future journal paper. The influence of CH_4 concentration is shown in Fig. 10d at several shock speeds with an ambient pressure of 133 Pa. The figure shows that increasing the CH_4 concentration from 2% to 5% increases the radiation intensity. However, if the CH_4 concentration is further increased to 8.6% CH_4, the radiation intensity decreases to the same level found in the 2% CH_4 case. The error bars shown in Fig. 10 correspond to the sum of the error due to the calibration and the error due to shot-to-shot variation. The error due to calibration is the most significant, and the level of this error affects all data points equally. Therefore, in terms of examining trends in the data, it is only the error due to the shot-to-shot variation that is significant as this is the only source of error that can change the intensity level of one data point relative to another.

The mechanism for increasing the freestream CH_4 concentration and decreasing the level of radiation intensity has been examined in a previous paper [1]. It was proposed that the methane dissociates into its constituent atoms immediately downstream of the shock and quickly forms CN through various exchange reactions with the atmospheric nitrogen. More methane available means more CN is produced. Therefore, at low-methane concentrations, the amount of radiation is proportional to the amount of methane in the atmosphere. As the amount of methane increases, another effect becomes important. The increased amount of methane decreases the postshock temperature because of dissociation [1]. So even though there are more CN molecules, the effective temperature at which the CN radiates is lower. Therefore, the net effect is to decrease the amount of CN radiation because the radiation intensity depends linearly on the number of radiating molecules but exponentially on the vibrational temperature [1].

V. Analysis

A. Flow-Quality Analysis

As the flow expands into the dump tank, the shock wave is bent by the interaction with the expansion fan wave structure resulting from the change in area, thus reducing the region of uniform core flow further downstream. This process has been modeled using a two-dimensional multiblock compressible Navier–Stokes (MB_CNS) solver [13]. The results of this analysis led to the assumption that the radiation is coming from a core radiating gas width of 60 mm [14,15]. By comparison, the EAST facility at NASA Ames Research Center

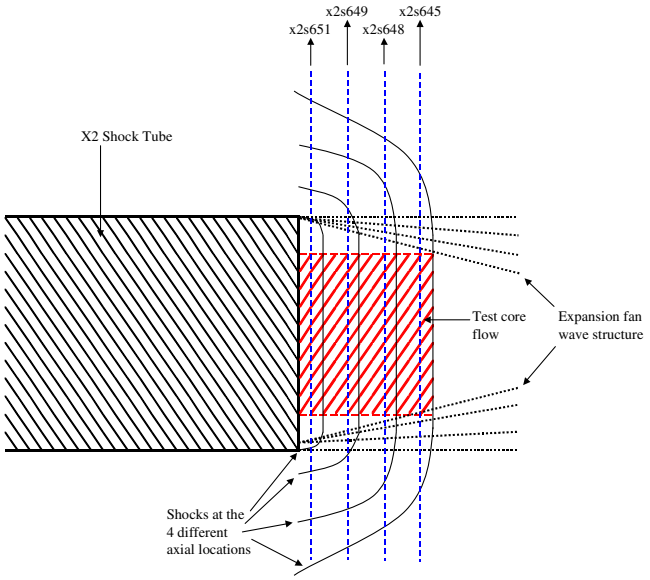

Fig. 11 Diagram showing the four shock positions and a representation of the effect of the expansion wave structure.

observes the radiating flow through windows in the shock tube with the radiation traversing the boundary layer on the wall.

If the expansion fan process was to have a significant effect on the measured radiation, the effect should increase the farther out of the tunnel the picture is taken. Therefore, four experiments were performed with the trigger system setup to take each picture 3 μs earlier than the last. At 5.7 km/s shock speed, this is equivalent to each shot being about 17 mm closer to the tunnel exit as detailed in Fig. 11. Figure 12 shows the wavelength profile obtained at the peak intensity location for each shot. The shots at the first three axial locations (x2s651, x2s649, and x2s648) are all within $\pm 2\%$ of each other when integrated across the wavelength spectrum. The shot taken at the last axial location (x2s645) was up to 8% less than the first three shots across when integrated across the wavelength spectrum. For the shots presented in this paper measuring the level of irradiance emitted from the flow, all were performed within the distance to the third axial location. Therefore, even though shot x2s645 was taken 51 mm farther out of the tunnel exit than x2s651, not only is the absolute level of intensity very similar, the wavelength profile also matches very well, indicating that near the tube exit a uniform core flow is maintained and the radiation from the

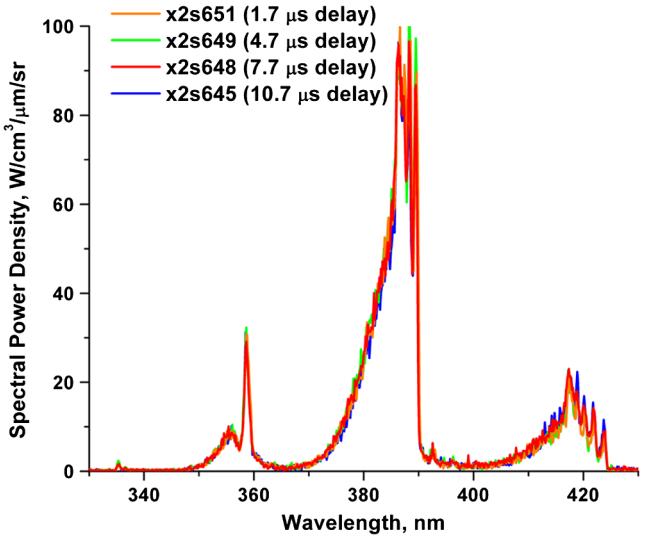

Fig. 12 Four shots repeated at 133 Pa, 5.7 km/s, and 98%N_2:2%CH_4 with different trigger delays.

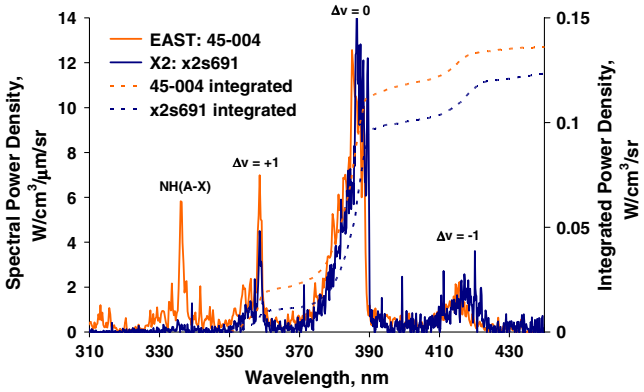

Fig. 13 Wavelength comparison of EAST [3] and X2 for Titan conditions at 5.7 km/s, 13 Pa, and 98%N_2:2%CH_4. The power density has been integrated over a wavelength range of 350–440 nm.

corner expansion and boundary layer is either not effecting the results or its effect is constant in the region of interest.

B. Comparison with NASA Ames EAST Facility

The facility and methodology behind both X2 and EAST testing is similar, and thus is a good source of data comparison, especially when it is considered that there are several common testing conditions. However, it is important to note there are two main differences between how the two facilities operate and measure radiation. On EAST, the radiation is analyzed through a window in the side of the shock tube, whereas in X2, the radiation is measured behind the shock after it exits the tunnel. This effectively means that on EAST, the radiation passes through the shock-tube boundary layer, whereas on X2, the radiation passes through an expansion fan-wave structure caused by the change in area as the flow propagates into the dump tank.

The other significant difference is the driver arrangement. X2 uses a free-piston driver, whereas EAST uses an electric arc-driven driver [3]. The advantage of the free-piston driver arrangement provides a cleaner interface between the test and driver gases and usually a more uniform test core flow, whereas the electric arc-driven driver arrangement can provide significantly faster speeds (up to 50 km/s).

The wavelength profile at the peak radiating condition obtained at 5.7 km/s, 13 Pa, and 98%N_2:2%CH_4 in the X2 facility has been compared to the equivalent data obtained in EAST (see Fig. 13).[¶] The absolute agreement between the two facilities is very good. However, the data shows that the CN $\Delta v = +1$ peak is slighter larger on EAST than X2, whereas the CN $\Delta v = 0$ and CN $\Delta v = -1$ peaks are slightly higher on X2. Further experimentation is required to determine which experimental results are best predicted by theory. The main difference between the two spectra, though, is that the peak at 336.3 nm [NH(A-X) transition], which is very prominent in the EAST data, is not significantly seen in the X2 data. The NH(A-X) transition is seen on X2 at a significantly lower intensity, as was shown in Fig. 6. However, there is no significant evidence of NH in the spectra shown in Fig. 13. This is due to the magnitude of the NH (A-X) transition at the peak radiating location being comparable to the magnitude of the noise in the experimental measurements. The spectra have also been integrated over a wavelength range of 350–440 nm to include the CN $\Delta v = -1, 0$, and 1 bands, but not the NH (A-X) transition. Although there are differences in the spectra, the agreement between the two facilities when the spectra are integrated is excellent, within 10%.

The power density integrated over the range of 340–440 nm has also been compared between both facilities and is presented in Fig. 14. The agreement is very good, with a 13% discrepancy in the absolute level of radiation at the peak, as seen in Fig. 14a. Figure 14a

[¶]The 5.7 km/s EAST condition was obtained from the NASA Ames Research Facility, which provided the data from their Titan experimental campaign.

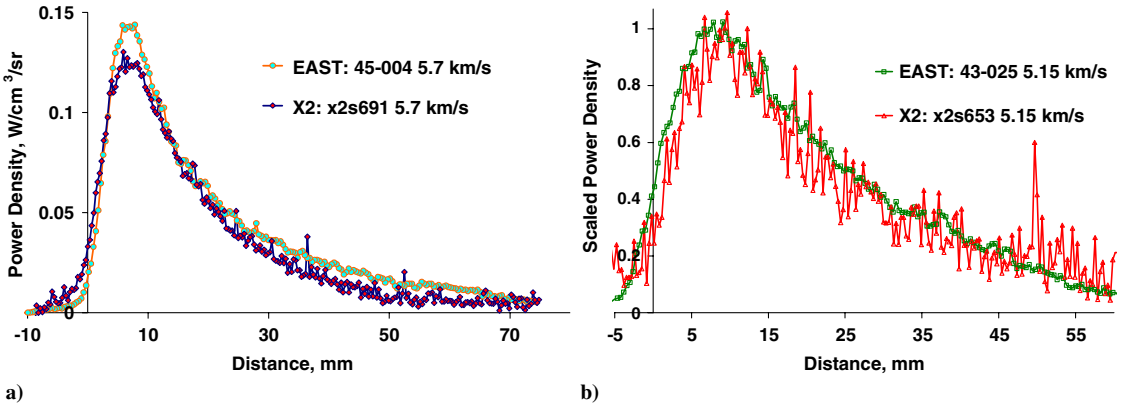

Fig. 14 Power density integrated over 340–440 nm comparison of EAST [3] and X2 for Titan conditions at a) 5.7 km/s, 13 Pa, and 98%N_2:2%CH_4 and b) scaled power density at 5.15 km/s, 13 Pa, and 98%N_2:2%CH_4.

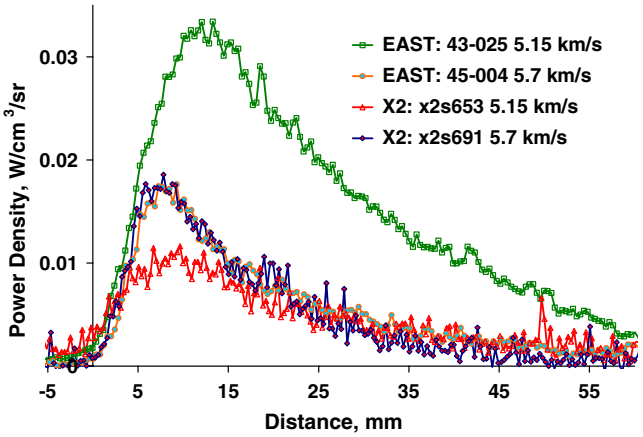

Fig. 15 Power density integrated over 400–430 nm comparison of EAST [3] and X2 for Titan conditions at 5.15 and 5.7 km/s, 13 Pa, and 98%N_2:2%CH_4.

shows the scaled power density for both EAST and X2 at the 5.15 km/s condition. The power-density decay rate is very important for the validation of CFD models and it can be seen that the agreement between the shots in terms of the decay rate is excellent. The reason for the increase in the level in noise in X2 is due to the shot having a significantly lower level of intensity and in this instance, a higher-resolution grating has been used for the EAST spectrometer. It should be noted that the X2 and EAST data has been shifted for ease of comparison. All shots have been shifted on the x axis so that they have the shock locations aligned with each other. This removes any superficial differences relating to the triggering of the data acquisition (e.g., gate delays or trigger pulse rise times).

A comparison of EAST and X2 for these two conditions, 5.15 and 5.7 km/s at 13 Pa, is shown in Fig. 15. Figure 15 shows that the 5.7 km/s shots agree very well between EAST and X2, both in terms of absolute levels and decay rates. However, there is a very significant difference between EAST and X2 at the 5.15 km/s condition, with the X2 data showing a power density less by a factor of approximately three. The X2 data shows a 37% decrease, whereas EAST shows a 91% increase when compared to the 5.7 km/s condition. Having a 0.55 km/s decrease in shock speed and finding a 91% increase in radiation intensity may indicate that the data from EAST shot 43-025 is anomalous, and thus may not be a suitable source for CFD validation purposes. Results from the EAST facility's Titan testing have been the focus of several groups attempts to simulate the radiation emitted from CN and for the development of collisional-radiative models [3,16,17]. One condition that has been common to all of these papers is the 5.15 km/s, 13 Pa, and 98%N_2:2%CH_4 condition performed in EAST [16–18]. However, because of the excellent agreement between the two 5.7 km/s shots, it appears that this condition would be better suited for CFD comparison.

VI. Conclusions

Large variations exist in predictions for radiation levels from CFD, and so experimental validation and a better understanding of the kinetics of CN-excited populations is required. We have shown calibrated intensity measurements for many different conditions for Titan entry. This data is very useful for heating load estimates for Titan entry, and also as a comprehensive data set for validating CFD models and understanding nonequilibrium radiating phenomena. Flow properties such as the evolution of temperature and vibrational populations in the flow could be calculated and compared to theoretical results. Furthermore, our experimental results for radiation intensity show very promising absolute agreement when compared to EAST under simulated Titan conditions. The condition also shows excellent flow data. The pitot trace is very steady, resulting in about 250 mm of radiating test gas (clearly verified by the high-speed camera) and the CN wavelength profiles have a very good noise-to-signal ratio for most conditions. Through the spectroscopic and shock-tunnel work conducted at The University of Queensland, significant insights into the Titan radiation problem have been achieved.

Acknowledgments

The experimental work in the X2 facility is supported by an Australian Research Council Grant and a Smart State Research Facilities Fund provided by the Queensland Government. Daniel Potter, Troy Eichmann, Fabian Zander, Andrew Dann, Matthew McGilvray, Mary D'Souza, David Gilfind, Carolyn Jacobs, Brian Loughrey, Keith Hitchcock, Eugene Kochnieff, and all the workshop staff for all their help and advice in conducting and setting up the experiments, optics, and data acquisition systems. Gary Allen, Joseph Olejniczak, Deepak Bose, Michael Wright, David Bogdanoff, and the group at NASA Ames Research Center for supplying the experimental data for the Enterprise Applications Service Technologies radiation testing campaign.

References

[1] Olejniczak, J., Wright, M. J., Prabhu, D., Takashima, N., Zoby V. E., Hollis, B. R., and Sutten, K., "An Analysis of the Radiative Heating Environment for Aerocapture at Titan," *Journal of Thermophysics and Heat Transfer*, Vol. 19, No. 1, 2005, pp. 17–27. doi:10.2514/1.10304

[2] Gnoffo, P. A., Weilmuenster, K. J., Hamilton, H. H., II, Olynick, D. R., and Venkatapathy, E., "Computational Aerothermodynamic Design Issues for Hypersonics Vehicles," *Journal of Spacecraft and Rockets*, Vol. 36, No. 1, 1999, pp. 21–43. doi:10.2514/2.3430

[3] Bose, D., Wright, M. J., Bogdanoff, D. W., Raiche, G. A., and Allen, G. A., Jr., "Modeling and Experimental Validation of CN Radiation Behind a Strong Shock Wave," *Journal of Thermophysics and Heat*

Transfer, Vol. 20, No. 2, 2006, pp. 220–230.
doi:10.2514/1.16869

[4] Johnston, C., Hollis, B. R., and Sutton, K., "Radiative Heating Methodology for the Huygens Probe," 9th AIAA/ASME Joint Thermophysics and Heat Transfer Conference, AIAA Paper 2006-3426, San Francisco, 2006.

[5] Osawa, H., Matsuyama, S., Ohnishi, N., and Sawada, K., "Comparative Computation of Radiative Heating Environment for Huygens Probe Entry Flight," *Journal of Thermophysics and Heat Transfer*, Vol. 22, No. 2, 2008, pp. 140–149.
doi:10.2514/1.31654

[6] Wright, M. J., Bose, D., and Olejniczak, J., "Impact of Flowfield-Radiation Coupling on Aeroheating for Titan Aerocapture," *Journal of Thermophysics and Heat Transfer*, Vol. 19, No 1, 2005, pp. 17–27.
doi:10.2514/1.10304

[7] Bogdanoff, D. W., "Shock Tube Experiments for Earth and Mars Entry Conditions," *Non-Equilibrium Gas Dynamics, from Physical Models to Hypersonic Flights*, VKI Lecture Series, Von Karman Inst. of Fluid Dynamics, Rhode-St.-Genèse, Belgium, 2008.

[8] Rond, C., Boubert, P., Felio, J., and Chikhaoui, A., "Experimental Investigation of Radiative Emission Behind a Strong Shock Wave in $N_2/CH_4/Ar$ Mixtures," *Journal of Thermophysics and Heat Transfer*, Vol. 21, No. 3, 2007, pp. 638–648.
doi:10.2514/1.28422

[9] Stalker, R. J., "Development of a Hypervelocity Wind Tunnel," *The Aeronautical Journal*, Vol. 76, June 1972, pp 376–384.

[10] Yelle, R. V., Strobell, D. F., Lellouch, E., and Gautier, "Engineering Models for Titan's Atmosphere," *Huygens: Science, Payload and Mission, Proceedings of an ESA Conference*, SP1177, ESA, Paris, 1997, pp 243–256.

[11] Mee, D. J., "Uncertainty Analysis of Conditions in the Test Section of the T4 Shock Tunnel," Dept. of Mechanical Engineering, Univ. of Queensland, Rept. 4/93, Brisbane, Australia, 1993.

[12] Kline, S. J., and McClintock, F. A., "Describing Uncertainties in Single-Sample Experiments," *Mechanical Engineering*, Vol. 75, No. 3, 1953, pp. 3–8.

[13] Jacobs, P. A., "A Computer Program for the Simulation of Transient Compressible Flows; 1998 Update," Dept. of Mechanical Engineering, Univ. of Queensland, Rept. 7/98, Brisbane, Australia, 1998.

[14] Potter, D. F., Gollan, R. J., Eichmann, T. N., McIntyre, T. J., Morgan, R. G., and Jacobs, P. A., "Simulation of CO_2-N_2 Expansion Tunnel Flows for the Study of Radiating Shock Layer,"AIAA Paper 2008-1280, 2008.

[15] Gollan, R. J., Jacobs, C. M., Jacobs, P. A., Morgan, R. G., McIntyre, T. J., Macrossan, M. N., Buttsworth, D. R., Eichmann, T. N., and Potter, D. F., "A Simulation Technique for Radiating Shock Tube Flows," *26th International Symposium on Shock Waves*, Paper 3531, Springer–Verlag, New York, 2007.

[16] Magin, T. E., Caillault, L., Bourdon, A., and Laux, C. O., "Nonequilibrium Radiative Heat Flux Modeling for the Huygens Entry Probe," *Journal of Geophysical Research*, Vol. 111, July 2006.
doi:10.1029/2005JE002616

[17] Hyun, S., Park, C., and Chang, K., "Rate Parameters for Electronic Excitation of Diatomic Molecules, 3. CN Radiation Behind a Shock Wave," *Journal of Thermophysics and Heat Transfer*, Vol. 23, No. 2, 2009, pp. 226–235.
doi:10.2514/1.36749

[18] Wright, M. J., Olejniczak, J., Walpot, L., Raynaud, E., Magin, T. E., Caillault, L., and Hollis, B. R., "A Code Calibration Study for Huygens Entry Aeroheating," 44th Aerospace Sciences Meeting and Exhibit, AIAA, Paper 2006-382, Reno, NV, 2006.

[19] McIntyre, T. J., Eichmann, T. N., Mallon, M., Potter, D. F., Brandis, A. M., Jacobs, C. M., Morgan, R. G., Jacobs, P. A., and Buttsworth, D. R., "The Generation and Measurement of High Temperature Radiating Flows in a High Enthalpy Pulsed Facility," *Proceedings of 3rd International Workshop on Radiation of High Temperature Gases in Atmospheric Entry*, Forth, Heraklion, Greece, 2008.